# Phase Transformations in Lipid A−Diphosphate Initiated by Sodium Hydroxide

Chester A. Faunce and Henrich H. Paradies*

The University of Salford, Joule Physics Laboratory, Faculty of Science, Engineering and Environment, Manchester M5 4WT, United Kingdom

ABSTRACT: The nature of the fluid phase transitions of charged-stabilized spherical lipid A−diphosphate clusters in aqueous dispersions was explored using a combination of small-angle X-ray scattering (SAXS) and electron microscopy. In contrast to previous studies, rather than removing NaCl, NaOH was added to the dispersions to promote crystallization. The fluid phase experiments were carried out employing titrations with $mM \cdot L^{-1}$ NaOH (c_S), along with variations in the particle-number density, n. When c_S was increased, a new fluid disordered phase of self-assembled lipid A−diphosphate was encountered, followed by a crystalline bcc phase and then a new fluid phase containing 70 nm lipid A−diphosphate particles. The bcc crystal structure found in this regime had a lattice constant of 35.6 nm. By varying c_S ($mM \ L^{-1}$), it was possible to determine the effective charge, $\overline{z}_{eff}$, for various n values and the screening parameter, k, for the excess electrolyte. For sufficiently large values of n, lipid A−diphosphate crystallized because of an increase in $\overline{z}_{eff}$ at a constant c_S. When the c_S was increased, the crystals melted with little change in $\overline{z}_{eff}$. The existence of a bcc−fluid phase transition for different values of c_S was supported by applying the Debye correlation function to the obtained data. An increase in c_S enhanced interparticle interaction and attraction. The effective charge and k accounted for counterion condensation and many-body effects. If the effective charge determined from scattering measurements was used in the simulations, the equilibrium phase boundaries were consistent with predicted universal melting-line simulations. At any particle-number densities, n, when the melting line was reached, 70 nm clusters were formed.
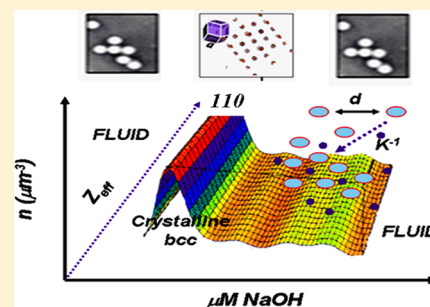
I. INTRODUCTION

Charged colloidal systems in aqueous dispersions are of considerable interest because of their relevance in the modeling of structures. This was seen for Yukawa-like systems where interactions occurred through a screened Coulomb potential that could be varied over a wide range, i.e., between the theoretical limits of a one-component plasma and a hard-sphere system.[1−6] The experimentally variable parameters were the particle-number density, n, the concentration of the screening electrolyte, c_S, and the effective charge, $\overline{z}_{eff}$. Measurements were made on variations of n and c_S, at low ionic strength, revealing a body-centered cubic (bcc) structure at low n and a face-centered cubic (fcc) structure at high n.[7−10] A complete phase diagram for charged spherical colloidal crystals was described by Sirota et al.[11] for low, moderate, and high n. A glass phase was also reported for the first time. A combination of computer simulations and scaled-particle theories showed that the range of the attractive part of the intermolecular potential determined whether or not the charged spherical colloid dispersion formed a stable liquid−liquid phase or a liquid−solid phase separation.[12] The bare particle charge was usually kept constant; the free counterions were determined from conductometry.[13] However, with an increased pH through the addition of NaOH, counterion condensation took place at large surface-charge densities.[14] If large surface-charge densities were involved, counterion condensation at the particle surfaces played a major role.[15−18] This was certainly the case in the

formation of charged micelles,[19−24] liposomes,[25] and model polymer systems grafted to the surface.[26]

Consistent with theory, the effective charge, $\overline{z}_{eff}$ saturated at a certain level, while Z, the bare charge, increased but with no gain in structure.[27] Robbins, Kremer, and Grest (RKG) analyzed the phase behavior of a Yukawa system by means of computer simulations[28] and observed universal melting lines for charged colloids. Meijer and Frenkel (MF)[29] predicted a lower melting line and lower crystal stability than RKG. The simulation results of Hamaguchi et al.[30] were between those of RKG and MF. In their crystallization studies of charge-variable systems, Palberg et al.[31] reported good agreements with the predictions of RKG. When the charge was taken from conductivity measurements, decreased crystal stability was noticed for large bare charges.[32] Recent research by Klein et al.[33] supported charge-like attractions and many-body effects, as shown for long-range interacting two-dimensional charged sphere fluids. A reduction in repulsion for such systems was attributed to macroion shielding.[33−35] Crystallization studies on these charge-variable systems were consistent with the calculations of RKG. In the absence of many-body effects, i.e., shielding, the superimposed potentials were assumed to be hard-core Yukawa-like potentials. If this were the case, the value of the effective charge would approach that of the experimental

conductivity charge. In the presence of shielding, an appreciably less steep potential well was displayed by the particle. When a hard-core Yukawa potential was applied, the shielding produced much lower values for the effective charge and elasticity charge.[36]

In addition, charged nano- and μm-sized lipid A−diphosphate clusters also influenced the stability and rheological properties of the system. Such changes in the properties of the system resulted from the segregation of domains near large uncharged colloidal lipid A−particles. This was previously observed for systems containing small to large spheres, large rods, or rods in the presence of spheres.[37,38] However, there is considerable interest in understanding the physical properties of lipid A−diphosphate dispersions during the titration process with bases, such as NaOH. Lipid A−diphosphate, the endotoxic principle of lipopolysaccharides (LPS) of Gram-negative bacteria, is the major component of the outer leaflet of the outer membrane, and its release in the course of bacterial infections is the cause of septic shock.[39−41] Therefore, the phase behavior of lipid A−diphosphate[42,43] is important for a variety of reasons which include production, stabilization, and detection of vaccines,[44−47] surface phenomena of membrane deformation,[48,49] biomineralization,[50] and multivalent anion binding.[51,52]

The present contribution goes beyond previous studies on the crystallization of noncovalently linked polymers, e.g., lipid A−diphosphate or lipid A−monophosphate.[53,54] From this investigation on self-assembled lipid A−diphosphate clusters, an increased understanding of the formation of highly ordered crystalline lipid A−diphosphate clusters and phases is foreseen. The lipid A−diphosphate cluster interaction was analyzed in a single self-contained system by tuning the charge on the clusters, with the addition of mM·L^{-1} NaOH solution (c_S). Using this method, a reliable and consistent mean field description was realized for the properties of charged lipid A−diphosphate clusters. Through the use of titration experiments utilizing mM·L^{-1} NaOH, a fluid phase transition was observed for this system and it was possible to study in detail much broader charge conditions than in previous work.[55]

It was also possible to monitor the freezing and melting regimes by means of an added electrolyte (mM·L^{-1} NaOH). The effective charge of the crystalline self-assembled lipid A−diphosphate clusters was determined from SAXS experiments. The SAXS results were taken from samples along the phase boundaries and compared with the charge obtained from the RKG predictions and from conductivity measurements. The crystalline−fluid phase transformation of the self-assembled lipid A−diphosphate cluster system required a transformation from an ordered-crystalline state to a fluid. This involved at least two phase transitions, initiated either by varying a single thermodynamic parameter (temperature) or by changing the chemical potential with the addition of hydroxyl ions.

The experimental procedures and simulations addressed in this investigation were as follows: (i) both phase and morphology transitions of self-assembled lipid A−diphosphate clusters were examined as a function of particle-number density, n, and the addition of a mM·L^{-1} NaOH (c_S); (ii) in the study, the particle charge was increased and the pH kept between $4.5 \leq$ pH ≤ 7.0; (iii) the main experimental techniques used in the investigation were electron microscopy, small-angle X-ray scattering (SAXS), and background electric conductivity, in order to estimate the conductivity charges; (iv) the experimental results obtained from the variations in the particle-number density, n, and c_S were analyzed following the simulation procedures of RKG.[28] The results were obtained without use of charge-like attraction explanations, where many-body effects were accounted for by the effective charges.

II. EXPERIMENTAL SECTION

A. Materials. All chemicals were of ACS analytical grade, and triple distilled water was used throughout for the solutions and dilutions. Aqueous solutions of NaOH were prepared by using ACS analytical grade NAOH (Fisher, U.K.) just prior to use; the concentrations were determined by conductometric titrations with HCl solutions. The dominant lipid A−diphosphate structures were produced from the (col+) *E. coli* strains, and were isolated, purified, and analyzed for composition by MALDI-TOF-MS (GSG GmbH, Karlsruhe, Germany) and LC-negative-ion spray mass spectrometry (HP 1100). The matrix for the MALDI-TOF-MS was sinapic acid. The preparation of transparent aqueous lipid A−diphosphate dispersions was according to previous protocols.[53,55] The chemical composition and integrity of the lipid A−diphosphate samples during the titration with μM NaOH was validated after each titration step with a MALDI-TOF MS, (LIMS), phosphorus and glucosamine content to detect any sample deterioration. The concentration by weight of solid lipid A−diphosphate was determined to be 0.5230 ± 0.00012 using an EG & G thermogravimetric analysis instrument. The conversion for units from mass fraction to constriction, c (μg/L), and volume fraction, ϕ, was determined by assuming a density of dry lipid A−diphosphate of 1.342 g/cm^3 ($\phi = cv_2$, with v_2 being the partial specific volume). Density measurements were made with a Paar DMA-02 densitometer (Graz, Austria).

B. Electric Conductivity. The protocol ensured identical interaction conditions for all experiments and measurements, including the determination of the effective charge of the samples by conductivity. Care was taken to avoid carbon dioxide contamination and ionic impurities originating from glass vessels by using a plastic apparatus. The determination of the apparent charges of the various aqueous lipid A−diphosphate dispersions was carried out by conductometric titrations and pH measurements with a Wayne−Kerr autobalance precision bridge (model B331) using micro-electrodes (25 ± 0.05 °C). The actual applied frequency was $\omega = 500$ Hz, a frequency which was low enough to carry out DC experiments at the limit. However, it was high enough to avoid electrophoretic lipid A−diphosphate particle transportation. The reproducibility of the conductivity measurements was found to be of the order of 8%.

A commercial device (Zeta-Sizer 4 Malvern) was used to assess the particle- surface charges, and the measurements were made at 25 °C. The average mobilities were determined from 20 measurements.

C. Electron Microscopy. Particle-size distributions were characterized by imaging the particles at a voltage of 20 kV using a scanning electron microscope (JEOL 6400) and at a voltage of 300 kV using a transmission microscope (JEOL 3010). The samples were withdrawn from the scattering cells under a light microscope (Olympus BX 60) and transferred to a substrate, coated with Pt (1 min), and studied in a SEM (JEOL 6400).

D. Small-Angle X-ray Scattering (SAXS). In dilute dispersions, interparticle interference was uncorrelated. The time averaged intensity $I(Q)$ was the sum of the scattered

intensities of the individual particles present in the dispersion. The form factor, $P(Q)$, describes the intraparticle interference, and for homogeneous spheres, it may be written as the sum over the phase differences according to eq 1

$$P(Q) = \left[\frac{3 \sin(QR) - 3QR \cos(QR)}{(QR)^3} \right]^2 \quad (1)$$

Experiments to obtain the particle-number density concentration of $30.0 \ \mu m^{-3} \leq n \leq 600 \ \mu m^{-3}$, which included data handling and processing, were performed as described previously.[53,55] After background corrections were made, a correction for the sample size vs the beam size (i.e., diffraction volume) together with an absorption correction was carried out at each data point. Each Bragg peak was then fitted with a Gaussian and integrated to obtain the intensity of the order peaks. An in-house modified Siemens D-5000 diffractometer was used to acquire the SAXS traces. The diffractometer was equipped with Goebel mirrors and with a thermostatically controlled sample holder for use in the temperature range 10–50 °C. SAXS was particularly useful in recording Bragg diffraction peaks in the wavevector region, $0.08 \ nm^{-1} \leq Q \leq 1.8 \ nm^{-1}$; the resolution was $dQ/Q = 0.03$ and the step size $\Delta Q = 0.02°$. Data were recorded for Q-values as low as $0.05 \ nm^{-1}$ (Cu Kα radiation, $\lambda = 0.154$ nm). The beam was K$_\alpha$/K$_\beta$ filtered and focused in the horizontal and vertical direction by total reflection from the Goebel mirrors. The relative variations in the intensities of the diffraction peaks in this region represented the absolute intensity values at low diffraction angles. For small Q-values, the 2θ separations between the reflections were within the accuracy of the measurements. The instrument may be connected to a CCD device (MAR USA, 0.064 mm pixel size, 13.5 cm) to observe the diffraction in real time, which facilitated the conversion of the scattered intensity to a 2θ plot. Readout noise on the CCD device and solvent scatter were subtracted from the accumulated data during the analysis. Accordingly, over the Q-range analyzed, the background scatter was uniform and estimated to be a constant. The liquid samples were placed in 1.5 mm thick cell holders surrounded by a Kepton film under an argon atmosphere for X-ray studies.

The particle-number density, n, of the colloidal lipid A–diphosphate dispersions was related to the volume fraction, ϕ, according to eq 2:

$$n = \frac{6\phi}{\pi \cdot \langle \bar{d} \rangle^3} \quad (2)$$

where $\bar{d}$ is the average lipid A–diphosphate diameter detected under the different experimental conditions with respect to c_S and n. The determination of the effective charge of the lipid A–diphosphate clusters rests on the structure factor $S(Q)$ and the interparticle potential. $S(Q)$ calculations were made by employing recent liquid-state theory.[56,57] $S(Q)$ was calculated from the particle-scattering intensity $I_p(Q)$ according to eq 3:

$$I_p(Q) = Kna^6 P(Q) \cdot S(Q) \quad (3)$$

Here $P(Q)$ is the form factor which is the square of the normalized scattering amplitude $P(Q) = f^2(Qa)$. K is a constant depending on the properties of the particles and of the solvent, where a is the radius of the assembled lipid A–diphosphate particle and n is the particle-number density. The quantity $Q = |Q|$ is related to the scattering angle θ by $Q = (4\pi/\lambda) \sin(\theta/2)$, where λ is the wavelength in the suspension. The structure

factor, $S(Q)$, for a system of interacting particles is represented in accordance with eq 4

$$S(Q) = 1 + \frac{4\pi \cdot n}{Q} \int_0^\infty [g(R) - 1] R \sin QR \ dR \quad (4)$$

Here $g(R)$ is the pair distribution function, n ($n = c/M$) is the particle-number density, and R is the center-to-center distance between particles. In a dispersion of noninteracting particles with a particle-number density n_0, $S(Q) = 1$, the average intensity $I_0(Q)$ for the reference suspension is $I_0(Q) = Kn_0 \cdot P(Q)$. Therefore, $S(Q)$ may be evaluated as a function of n and is accessible at a large amount of the c_S where particle–particle interactions are suppressed and $I_p(Q)$ is the averaged intensity $I(Q)$.

The interpretation of the SAXS results for colloidal suspensions may be influenced by the polydispersity in size, shape, and charge. In the absence of interactions, it can be treated using the integral form of eq 5:[58]

$$I_p(Q) = K \sum_{ij} \sqrt{c_i c_j M_i M_j f(Qa_i) f(Qa_j) S_{ij}(Q)} \quad (5)$$

where a_i, $M_i \propto a_i^3$, and $c_i = n_i M_i$ are the average radius, molecular weight, and weighted average molecular weight of species i and the $S_{ij}(Q)$ are the partial structure factors (eq 6):

$$\bar{S}(Q) = \frac{1}{P(Q)} \sum_{i,j}^m f_i(Q) \cdot f_j(Q) \cdot S_{i,j}(Q) \quad (6)$$

In the limit for weakly interacting particle systems, $S_{ij}(Q) = \delta_{ij}$, therefore, eq 7 is valid:

$$I_{p,o}(Q) = K \sum_i n_i M_i^2 P_i(Q)$$
$$= K \int_O^\infty n(x) M^2(x) f^2(Qx) \ dx \quad (7)$$

where $n(x) \ dx$ represents the number of particles per unit volume, with a radius between x and $x + dx$ in dilute systems. The polydispersity is treated using the integral form of eq 8, assuming a Gaussian distribution for $n(x)$:

$$n(x) \propto \exp\left[-\frac{1}{2} \left(\frac{x - a}{\sigma} \right)^2 \right] \quad (8)$$

Here a is the average size of the particle and σ is the width of the distribution. The polydispersity in the lipid A–diphosphate particle-size distribution was characterized by the relative standard deviation σ^2, which was in the order of $0.10 \leq \sigma \leq 0.20$. These values were within the range of the experimentally probed wavenumbers. A three-component system was found satisfactory for the structure factor calculations. If interactions were present in polydisperse suspensions, they were represented by a three-component mixture of sizes, $a - \sigma$, a, and $a - \sigma$ with relative number densities of 1, 2, and 1. The equilibrium pressure, compressibility, and structural properties of $S_{ij}(Q)$ were obtained from liquid-state theory. The height of the first $S(Q)$ peak was calculated using the hypernetted chain approximation (HCNA) with the Rogers–Young closure.[59] For the various particle-number densities of lipid A–diphosphate, the appropriate mixing parameters were used in such a way that $\chi_T^{(f)}$ and $\chi_T^{(v)}$ computed from the fluctuation and virial expressions coincided. Applying a primitive model, all mutual correlations between macroions (lipid A–diphosphate) and the
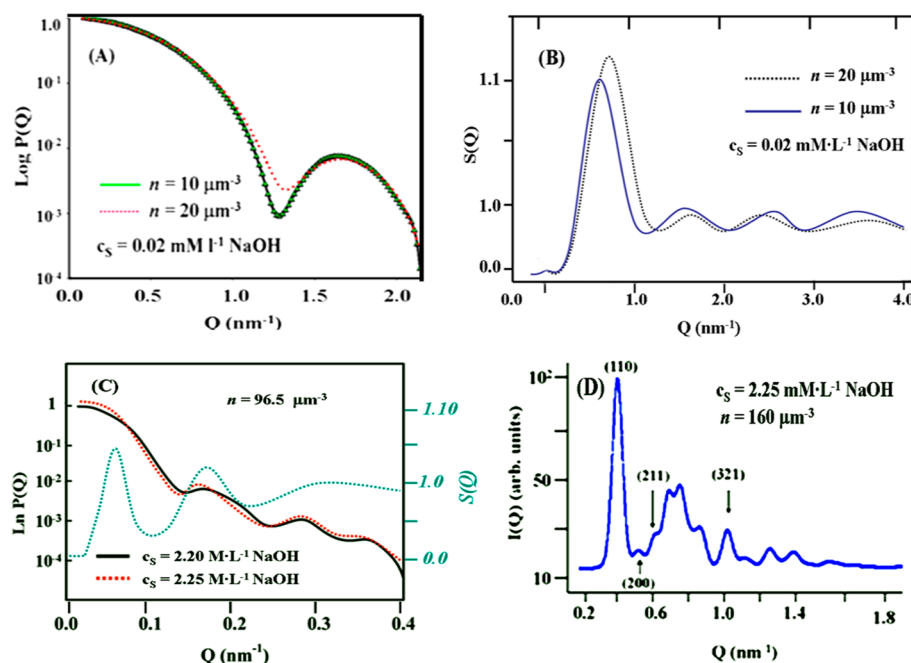
Figure 1. (A) Form factor profiles obtained from SAXS measurements for lipid A−diphosphate clusters at $n = 10 \ \mu m^{-3}$ (▲▲▲) experimental, and the solid (—) line is the form factor curve fitted to a Gaussian polydispersity of 8.9% and $R = 3.50 \pm 0.05$ nm. The dotted (⋯) red line is the SAXS profile for the sample containing 20 μm^{-3}. Both samples contained 0.02 mM L^{-1} (25 °C). (B) The corresponding $S(Q)$ vs Q profiles from SAXS experiments for $n = 10 \ \mu m^{-3}$ (—) and 20 μm^{-3} (⋯) and $c_S = 0.02$ mM L^{-1} at 25 °C. (C) SAXS profiles obtained for lipid A−diphosphate clusters for $n = 96.5 \ \mu m^{-3}$ and after titration with $c_S = 2.25$ (⋯) and 2.00 (—) mM·L^{-1} NaOH. The best form factor fits for $P(Q)$ vs Q and a value of $R_G = 27.6 \pm 0.8$ nm determined from the Guinier approximation. The corresponding $S(Q)$ vs Q profiles from SAXS experiments for $n = 96.5 \ \mu m^{-3}$ (—) and $c_S = 2.25$ mM L^{-1}. (D) Diffraction pattern of the polycrystalline lipid A−diphosphate clusters ($n = 160 \ \mu m^{-3}$ and $c_S = 3.10$ mM·L^{-1} with a bcc structure and a lattice constant of $a = 35.7$ nm. The assigned space group was $Im3m$ (origin at the center $m3m$ and equivalent positions 0, $^1/_2$, $^1/_2$; $^1/_2$, 0, $^1/_2$; $^1/_2$, 0, Q^{229}).[61]

salt electrolyte ions (OH$^-$ and Na$^+$) interact through the Coulomb potential. The screening of the bare Coulomb interactions by the salt ions resulted in a mean force potential $U(r)$ between the macroions that depended on both the charge and the particle-number density of the macroions. However, different structures possessed different radii a_μ and a_ν and also had different charges Z_μ and Z_ν. Consequently, an increase in the polydispersity resulted in both a reduction in the main $\overline{S}(Q)$ peak and a movement of the peak toward a higher Q value. For systems that were moderately polydisperse, the interaction potential between particles exhibited radii of a_μ and a_ν and effective charges Z_μ and Z_ν; therefore, the ion-averaged DLVO-like potential between particles[60] may be written as eq 9:

$$U_{\mu\nu}(r) = \frac{Z_\mu Z_\nu e_0^2}{4\pi\varepsilon_r\varepsilon_0} \frac{e^{ka_\mu}}{1 + ka_\mu} \frac{e^{ka_\nu}}{1 + ka_\nu} \frac{e^{-kr}}{r}; \quad r > a_\mu + a_\nu$$

$$= +\infty; \quad r < a_\mu + a_\nu$$

(9)

where the screening constant is $k = (2e^2 I/\varepsilon\varepsilon_0 \cdot k_B T)^{1/2}$. The ionic strength, I, includes the salt ions (I_S), the counterions, which equilibrate the colloidal charge, and Z_i, the number charge of the colloid i according to eq 10:

$$I = I_S + \frac{1}{2}\sum_i Z_i \rho_i$$

(10)

This multicomponent model (MCM) was solved for the lipid A−diphosphate suspensions by applying the HCNA and using a three-component mixture of sizes $a - \sigma$, a, and $a + \sigma$, with number densities of 1, 2, and 1 in the presence of mM·L^{-1}

NaOH. Larger particles contributed appreciably to the scattering intensity at low scattering angles, even when the lipid A−diphosphate particle numbers were small. Since the scattering amplitude also depended on the scattering-length distribution of the three-component sample, the compressibility of each individual sphere contributed to $\overline{S}(Q)$.

The effective structure factor $\overline{S}_{eff}(Q)$ was defined from the experimental SAXS scattering intensities similar to that of a one-component fluid according to eq 11:[58]

$$\overline{S}_{eff}(Q) = \frac{I_p(Q)}{I_{p,0}(Q)}$$

(11)

Here, $I_{p,0}(Q)$ is the scattered-light intensity of a sample of noninteracting particles with a particle-number density of n_0. Both $I_p(Q)$ and $\overline{S}_{eff}(Q=0)$ are calculated using liquid-state theory. Since the measurements are carried out in a dilute concentration regime, it is acceptable to work in arbitrary units. $\overline{S}_{eff}(Q)$ is then calculated using $I_{p,0}(Q)$, which can be taken directly from the scattered intensity. This is acceptable because $\overline{S}_{eff}(Q=0)$ for each n is calculated by extrapolating the measured values of $\overline{S}_{eff}(Q)$ to $Q = 0$. The radii, a_μ, and the number densities, n_μ ($\mu = 1, ..., n$), of the solution components are chosen in such a way that the first $2m$ moments of the histogram distribution coincide with those of the original histogram distribution. The scattering amplitude is then the weighted sum of the contributions of the individual components, e.g., $I(Q) \propto \overline{P}(Q) \cdot \overline{S}(Q)$. This is analogous to the monodisperse case, because the normalized scattering intensity $I(Q)$ no longer factors into parts that depend only on single-particle properties or the interparticle correlations. The
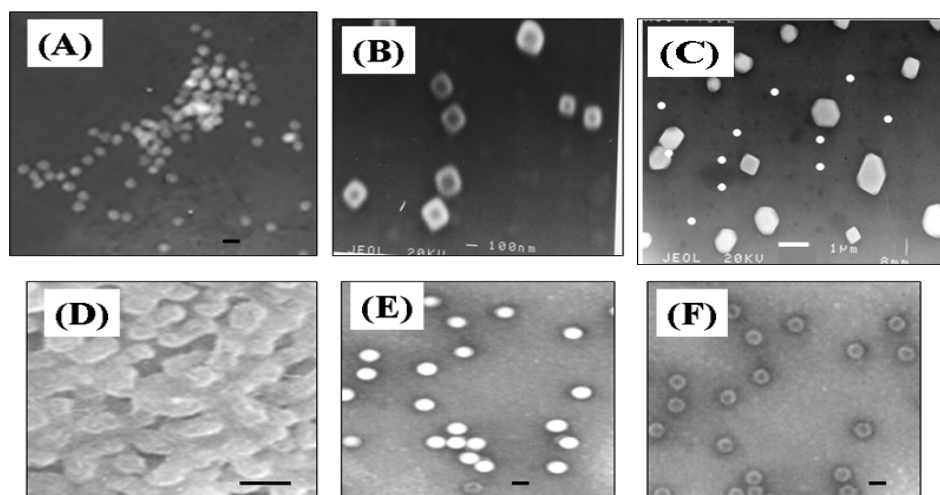
Figure 2. (A) TEM image of lipid A−diphosphate clusters of diameter $d \sim 6.6$ nm observed in the fluid phase, $c_S = 0.0−0.05$ mM·L^{-1} and $n = 96.5$ μm^{-3}. The scale bar is 10.0 nm. (B) SEM image of crystals formed at $c_S = 1.0$ mM·L^{-1} and $n = 120.5$ μm^{-3}. The scale bar is 100 nm. (C) SEM image of single lipid A−diphosphate crystals; some 6.6 nm clusters are also present, $c_S = 2.0$ mM·L^{-1} and $n = 130$ μm^{-3}. The scale bar is 1 μm. (D) SEM image for $c_S = 1.35$ mM·L^{-1} and $n = 96.5$ μm^{-3} near the melt boundary. The scale bar is 100 nm. (E) TEM image of single lipid A−diphosphate clusters with $d \cong 66$ nm for $c_S = 5.25$ mM·L^{-1} and $n = 96.5$ μm^{-3}. (F) A TEM image of lipid A−diphosphate clusters with $d \cong 70$ nm but for $c_S = 4.25$ mM·L^{-1} and $n = 48.0$ μm^{-3}. The scale bars in parts E and F are 50 nm.

quantity $\overline{P}(Q)$ is the form factor averaged over the size distribution, and $\overline{S}(Q)$ is the measured structure factor, which contains single particle quantities, e.g., the normalized scattering amplitude. To avoid arbitrary shifts in $\overline{S}(Q)$, the scattering intensities were analyzed for their asymptotic behavior at large Q values. The structure factor $\overline{S}(Q)$ was obtained by normalizing the reduced intensity $I(Q)/\overline{P}(Q)$ at its highest accessible Q. Convergence was verified by using the oscillating part of $I(Q)/\overline{P}(Q)$ at low scattering angles. The $\overline{S}(Q)$ values were calculated for $Z_\mu \propto a_\mu$, keeping the average charge constant. The values calculated for monodispersed lipid A−diphosphate clusters with $a = 35.6$ nm in the absence of salt were as follows: $\chi_T^{(v)} = 0.010$, $S_{eff}(0) = 0.0098$, and $\pi/\rho \cdot k_B = 113.7$. The corresponding values for a polydisperse system with $m = 3$, $a = 35.6$ nm, and $2\sigma = 5.0$ nm were 0.0095, 0.0094, and 100.0, respectively.

III. RESULTS AND DISCUSSION

A. SAXS and Electron Microscopy. Figure 1A illustrates the intensity scattering profiles plotted as $P(Q)$ vs Q obtained from SAXS measurements of lipid A dispersions at low particle-number densities $n = 10$ and 20 μm^{-3} at $c_S = 0.02$ mM·L^{-1}. Figure 1B shows the corresponding structure factor $S(Q)$ vs Q profiles for $n = 10$ and 20 μm^{-3} at $c_S = 0.02$ mM·L^{-1}. In Figure 1C are the $P(Q)$ form factor profiles vs Q for particle-number density $n = 96.5$ μm^{-3} and for $c_S = 2.25$ and 2.00 mM·L^{-1} obtained from SAXS measurements. The experimentally determined radius of gyration $R_G = 2.92 \pm 0.07$ nm shown in Figure 1A was used to normalize the form factor, taking into account a polydispersity of 8%. The experimental values exhibited an excellent fit to the scattering curves $P(Q)$ vs Q and $S(Q)$ vs Q (Figure 1A and B). The structure factor peak $S(Q)$ occurred at $Q \sim 1.2$ nm^{-1} (Figure 1B), and the low intensity value of this peak was a result of interactions in both dilute conditions and low mM·L^{-1} NaOH concentrations.

The calculated and experimental $P(Q)$ vs Q profiles correspond to a uniform spherical lipid A−diphosphate cluster with $R_G = 27.6$ nm ($R_H = 35.6$ nm). Figure 1D reveals a diffraction profile of polycrystalline lipid A−diphosphate

clusters for $n = 160$ μm^{-3} and $c_S = 3.10$ mM·L^{-1} at 25 °C. From the profile (Figure 1D), the higher order Bragg peaks of a bcc lattice were in evidence and the lattice constant $a = 35.7$ nm was determined. For a polydispersity between 8 and 9.5%, no difference was found between the calculated and experimental form factor vs Q plot. Neither high c_S nor n appreciably affected the scattering or the chemical integrity of the lipid A−diphosphate. The identification of several orders of Bragg peaks facilitated an unambiguous determination of the crystal structure and the lattice constant as a function of c_S. The derived structures were based entirely on the location of the Bragg peaks, which included the indexing of the bcc crystal (Figure 1D). From an analysis of the intensity profiles, including those for high values of Q, along with the successful indexing of the Bragg peaks, a space group $Im3m$ was assigned. Because the seventh order Bragg peak (321) was present, it is possible to differentiate between a bcc and a primitive cubic (sc) lattice, since the (321) reflection is absent from the primitive cubic structure. The intensity of the third order Bragg peak (211) after deconvolution exceeded that of the second order Bragg peak (200). The form factor $P(Q)$ decreased with Q in this Q-region, and the degeneracy of the third-order Bragg peak exceeded that of the second-order Bragg peak. This showed that in the powder diffraction profile of a bcc structure there is higher degeneracy in the third-order Bragg peak than in the corresponding peak of the primitive cubic structure. Therefore, it was deemed possible to monitor the (110) reflection as a function of c_S and n.

Figure 2 shows a number of electron microscopic images for lipid A−diphosphate samples with different NaOH concentrations, c_S, and particle-number densities, n. In Figure 2A are a loose distribution of spherical lipid A−diphosphate clusters of diameter $d \cong 7.0$ nm observed for $c_S = 0.0−0.05$ mM·L^{-1} and $n = 96.5$ μm^{-3}, with no crystalline material present. Figure 2B shows lipid A−diphosphate crystals visible in SEM images for $c_S = 1.0$ mM·L^{-1} and $n = 96.5$ μm^{-3}, with crystallite sizes between 0.05 and 0.5 μm. Figure 2C shows large lipid A−diphosphate single crystals appeared at $c_S = 2.0$ mM·L^{-1} and $n = 130$ μm^{-3} together with some spherical lipid A−diphosphate clusters of
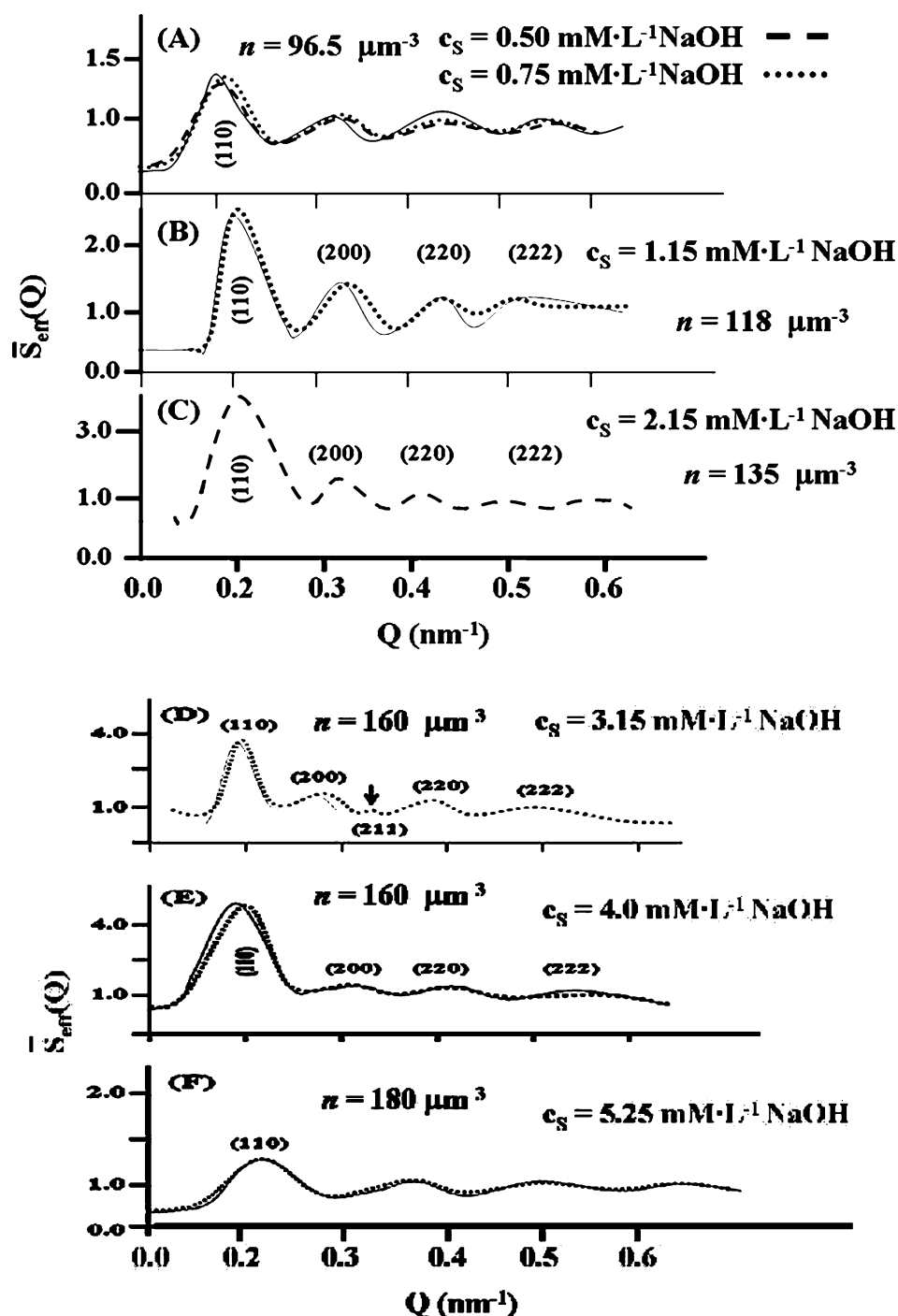
Figure 3. Scattering profiles for $\overline{S}_{eff}(Q)$ vs Q obtained from SAXS as a function of c_S for lipid A−diphosphate clusters with different particle-number densities all at 25 °C: (A) $n = 96.5.5$ μm^{-3}, the dotted (⋯) and the dashed (- - -) lines are from measurements of $c_S = 0.5$ and 0.75 mM·L^{-1}. The solid black line is the calculated line for the crystalline bcc lipid A−diphosphate clusters with $a = 37.5$ nm. Parts B−F show the $\overline{S}_{eff}(Q)$ vs Q profiles for increasing c_S at the indicated lipid A−diphosphate particle-number density, n. The solid lines are the calculated lines for the crystalline bcc lipid A−diphosphate clusters with $a = 35.7$ nm and the (110), (200), (211), etc., spacings with $\rho = 11.5\%$, $z_{eff} = 400$, and $\sigma = 10\%$.

diameter $d \cong 7$ nm. Figure 2D shows that, approaching the melt boundary at 1.35 mM·L^{-3} NaOH and $n = 96.5$ μm^{-3}, the crystal morphology is more rounded with few sharp facets unlike the lipid A−diphosphate crystals in Figure 2B and C. Figure 2E shows isolated but uniform lipid A−diphosphate clusters of diameter $d \cong 70$ nm at $c_S = 5.25$ mM·L^{-1} and at the same particle-number density $n = 96.5$ μm^{-3}. The clusters were similar in shape to those observed under the conditions found in Figure 2A. However, these clusters were 10 times larger (70

nm) and showed no crystalline material. In Figure 3, SAXS traces are presented for a number of particle-number densities, n, and for various c_S. The positions of the first $S_{eff}(Q)$ peaks were constant to within 5%. However, there was a significant increase in the magnitude of the peaks with a rise in n, however, at variance with the addition of c_S (μM NaOH). Evaluation of the peak widths at half-height of ΔQ were measured according to Warren[62,63] to obtain the average dimensions of the lipid A−diphosphate nanocrystals. Here, the equation $A = 2\pi K \Delta Q^{-1}$

with $K = 1.075^{64}$ yielded A values between 1.5 and 0.050 μm. The intensity profiles $I(Q)$ and $S(Q)$ of the lipid A−diphosphate samples were interpreted as the summation of a bcc crystalline phase and a disordered liquid, showing the coexistence of two phases.[65]

B. Structure Factor. SAXS profiles were recorded at a constant particle-number density, n, as a function of c_S (25 °C). Theoretical $\overline{S}_{\text{eff}}(Q)$ vs Q profiles were generated from experimentally acquired $I(Q)$ vs Q data for $n = 135.5$ μm^{-3}, as a function of c_S (Figure 3), using the effective charge $\overline{z}_{\text{eff}}$ and a polydispersity of 8.5% (Table 1). The effective structure

Table 1. Lipid A−Diphosphate Cluster Parameters Using the Poisson−Boltzmann Cell Model (PBC) and the Charge Regulation Model for c_S = 2.55 mM L^{-1} and α = 5.5 × 10^{-3} (25 °C)^a

parameter	quantity	parameter	quantity
$\overline{2a}$ (nm)	70.5 ± 0.8	σ_a (μS/cm^2)	0.804 ± 0.01
R_G (nm)	27.6 ± 0.7	σ_{eff} (μS/cm^2)	0.12 ± 0.01
ρ (%)	8.5 ± 0.7	Φ_0 (mV)	−175.5
Z_P	1245 ± 190	pK_a	2.35 ± 0.06
Z_σ	470 ± 100	pH$_0$	1.92 ± 0.06
$\overline{z}_{\text{eff}}$	390 ± 120	c_S (F/m^2)	0.31

^{a}$\overline{2a}$ is the mean average diameter of the lipid A−diphosphate cluster determined from TEM, SEM, and SAXS; R_G is the radius of gyration determined from SAXS experiments; ρ (%) is the averaged polydispersity determined from SAXS measurements; Z_P is the titrated charge; Z_σ is the mean conductivity charge; z_{eff} is the mean effective charge derived from the PBC model; σ_a and σ_{eff} are the analytical and effective charge densities, respectively; the quantity α (=[R−HPO$_4^-$]/[R−H$_2$PO$_4$]) is the degree of dissociation of the inorganic phosphate groups; Φ_0 is the electrostatic surface potential; c_S is the Stern capacitance; pK_a is the apparent pK of the phosphoric acid groups; pH$_0$ is the surface concentration of the protons which is related to the bulk proton concentration ([H$^+$]$_B$) by the surface potential Φ_0 according to [H$^+$]$_0$ = [H$^+$]$_B$ e$^{-\Phi_0}$.[18]

factor $\overline{S}_{\text{eff}}(Q)$ (eqs 6 and 11) was compared with the experimental scattering data, which fitted both peak position and peak height, e.g., the (110) and (200). Good overall agreement was found between the experimental and calculated values. In Figure 3C−E, the heights of the (110) $S(Q)$ peaks were observed to be between 4 and 4.5. However, in Figure 3F, a dramatic reduction in the height of the $\overline{S}_{\text{eff}}(Q_{110})$ peak was noticed as well as a shift in the peak position to a higher Q-value. Using a model, where spheres occupy the lattice sites of the 70 nm bcc cubic lipid A−diphosphate crystal, it was possible to quantitatively describe the Q-dependence of the $\overline{S}_{\text{eff}}(Q)$. This was accomplished by the deconvolution of the average $\overline{S}_{\text{eff}}(Q)$ curve into two components, the 70 nm particles and the crystalline bcc assembly through the use of eqs 6−8. Using a model where spheres occupy the lattice sites of the 70 nm bcc cubic lipid A−diphosphate crystal, it was possible to quantitatively describe the Q-dependence of the $\overline{S}_{\text{eff}}(Q)$. This was accomplished by the deconvolution of the average $\overline{S}_{\text{eff}}(Q)$ curve into two components, the 70 nm particles and the crystalline bcc assembly through the use of eqs 6−8. This deconvolution supports the appearance of the 70 nm particle ($Q \cong 0.089$ nm^{-1}) after an increase of $c_S = 5.25$ mM·L^{-1} NaOH for $n = 180$ μm^{-3} and the disappearance of the bcc crystalline structure at $Q \cong 0.20$ nm^{-1}. According to the rule of Verlet and Hansen,[66,67] crystallization occurs when the structure factor of ordinary liquids exceeds a value of 2.85. For the (211) peak at

c_S = 3.15 mM·L^{-1}, if c_S was held constant, it was observed that the height of the reflection increased with the particle-number density (Figure 4). When plotted on a double-log graph, a value
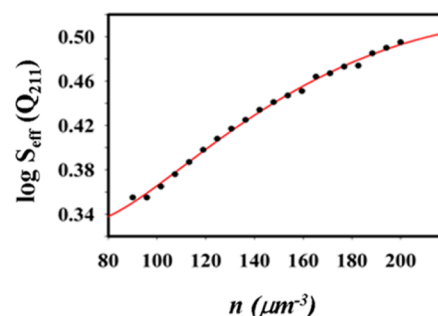
Figure 4. Fractal growth of $\overline{S}_{\text{eff}}(Q)$, the structure factor peak of the (211) reflection as a function of the particle-number density, n (d_f = 1.75, the sticking probability was $p = 0.04$) at c_S = 3.45 mM·L^{-1}. (●) Experimental; (—) theoretical with $I(Q) = S(0)/[+(QR_G)^2/3/2·d_f]^{d_f}$ for $QR \gg 1.0$).[70]

of d_f = 1.75 was obtained. This result may explain why the lipid A−diphosphate basic arrays adopted the form of colloidal clusters at these particle-number densities and for low values of c_S. The number of seeding lipid A−diphosphate clusters of $\overline{d}$ = 7 nm required to form a fractal nucleus of a given size was considerably lower than the number required for a compact nucleus. These parameters determined whether or not small clusters or subcritical nuclei developed. Once formed, further cluster growth took place if a sufficient supply of lipid A−diphosphate clusters of $\overline{d}$ = 7 nm were available. The correlation length ξ ($\xi = 2\pi/Q_{211}$) became significantly smaller with an increased $c_S = 3.15$ mM·L^{-1}; the Q_{211} position moves to a higher Q value and increased with decreasing sticking probability. For $p = 0.04$, the SAXS intensity $I(Q_{211}) \propto Q_{211}^{-d_f}$, yielding a value of $d_f = 2.05$ which was within the range of $2\pi/\xi \leq 2\pi/a$. Therefore, cluster growth depended upon the particle-number density and the size and the charge polydispersity as well as the availability of residual lipid A−diphosphate clusters. A further increase in the NaOH concentration resulted in crystal melting which produced a fluid phase containing the 70 nm clusters. The nearest-neighbor interparticle distance, $2d_{\text{exp}} = 2\pi/Q_{110} = 32.2$ nm, was estimated from the experimental peak positions and compared well with the average theoretical distance, $2d_{\text{th}} = \sqrt{3}/(4n)^{1/3}$, for various particle-number densities, 20 μm$^{-3} \leq n \leq 200$ μm^{-3}. For this limited particle-number density range, the double-logarithmic plot of $2d_{\text{exp}}$ and $2d_{\text{th}}$ vs n revealed a straight line with a slope of −0.32. The nearest-neighbor distance in the fluid phase was determined as $d_{\text{N−N}} = 33.0$ nm.

The random packing density for the 70 nm particle in the fluid phase was high and possibly exceeded the crystal packing in the crystalline bcc phase, making crystallization less favorable entropically. The surface vertices of the 7.0 nm particle when packed within the 70 nm particles experienced a face-to-face contact, which kinetically hindered crystallization. Similarly, rotator phases can be considered where an ordered crystal or quasicrystal retained translational order but exhibited dynamical orientational disorder.[68] The nearest-neighbor distance for the fluid phase before freezing was found to be $d_{\text{N−N}} = 32.2$ nm when a homogeneous particle distribution was assumed with cubic bcc symmetry. The observed intersphere spacing was normally close to the calculated mean sphere distance except at

the interfacial region of the dispersions, where there was contact with the air or a wall. Melting was initiated when the amplitude of vibration became sufficiently large for the occurrence of partly shared occupancy between adjacent particles. It occurred when the root-mean-square of the amplitude of vibration exceeded a threshold value ($\sim 0.15 d_{N-N}$).[69] This resulted in a movement of $\sim$5.5 nm, which was a distance significantly smaller than the spacing between the surfaces of the spherical colloidal lipid A−diphosphate clusters and a distance much less than the screening length. In addition, the possibility exists that the charge deduced from the melting line was also essential to center the particle within the cubic bcc unit cell.

Figure 5A shows SAXS profiles for lipid A−diphosphate dispersions for $n = 120$ μm^{-3} for two concentrations of NaOH
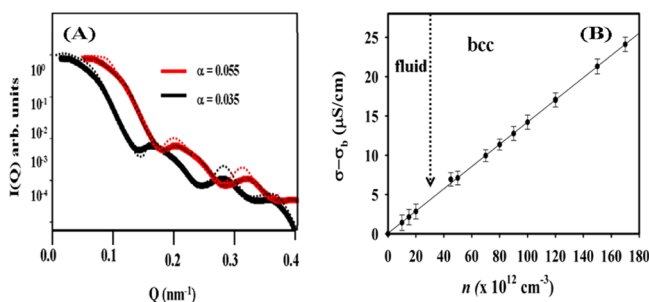
Figure 5. (A) SAXS profiles from dispersions of lipid A−diphosphate cluster with $n = 120$ μm^{-3} and $c_S = 2.15$ mM·L^{-1} NaOH (black line) and $c_S = 5.15$ mM·L^{-1} NaOH (red line). Applying $\alpha = 0.035$ (2.15 mM·L^{-1} NaOH) and $\alpha = 0.055$ (5.15 mM·L^{-1}) as the degree of dissociation of the phosphate group (p$K_{a1} = 2.35$). The dotted lines represent the theoretical scattering fits for spherical particles with $d = 70$ nm and $z_{eff} = 390$ for a three-component system. The red curves are shifted horizontally for perspicuity. (B) A background corrected conductivity curve for dispersions of lipid A−diphosphate clusters as a function of the particle-number density n covering the investigated concentration range. The background conductivity σ_b was assessed to be 1.65×10^{-6} mol/L. The vertical line indicates the estimated position of the fluid−solid phase boundary.

and for two values of $\alpha = [\text{R}-\text{HPO}_4^-]/[\text{R}-\text{H}_2\text{PO}_4]$. The very small degree of dissociation of the phosphoric acid groups along with the measured conductivity as a function of n at constant c_S were shown in Figure 5B.

The scattering profiles were similar at low Q scattering vectors, but there were minor variations at slightly higher Q values ($Q \geq 0.45$ nm^{-1}). No detectable changes in the value of R_G were found even if two different values of α were applied to fit the experimental scattering curve.

This was a completely different conclusion than those drawn from a previous experiment where NaCl was removed, revealing values of $\alpha = 0.20-0.22$.[53] The size of the hydroxide ion, its mobility,[71] and the presence of the Na$^+$ were all involved in the neutralization of the charges of the lipid A−diphosphate clusters.

In Figure 5B, the background corrected low frequency conductivity was plotted as a function of n (20 $\mu m^{-3} \leq n \leq 200$ μm^{-3}) at $c_S = 1.65 \times 10^{-6}$ M·L^{-1}. The curve showed a linear increase in low frequency conductivity with an increase in the particle-number density. The conductivity of the lipid A−diphosphate dispersions was wholly dependent upon the ionic species in the aqueous dispersion. Therefore, the conductivity was not influenced by the solid state phase transition. For a

sufficiently large particle-number density, n, the mobility of the cluster became independent of n ($\sim$15 μm S^{-1}/V cm^{-1}).

C. Effective Charge. A comparison was made between the electro-kinetic charge and the effective charge before and after the addition of $c_S = 5.15$ mM·L^{-1}. The comparison was achieved by an examination of the $S_{eff}(Q)$ results extracted from the SAXS experiments for 20.0 $\mu m^3 \leq n \leq 250$ μm^3 (Figure 3). A three-component polydispersity model was then used applying two parameters, the average cluster size and the standard deviation in the lipid A−diphosphate cluster size. Therefore, the assumption was made that a relationship between the effective charge of the subcomponent μ and the size of the subcomponent σ_μ could be established in accordance with (eq 12):[72]

$$Z_\mu^{eff} = \overline{Z^{eff}} \left(\frac{\sigma_\mu}{\overline{\sigma}} \right)^\alpha \tag{12}$$

Here Z_μ^{eff} is the mean effective charge and the exponent α may be evaluated from a comparison of the experimental and calculated $S(Q)$ values. Even if their cluster numbers were small, larger clusters made a significant contribution to the scattering intensity at low scattering angles. Consequently, the scattering amplitude (B_μ) of each individual sphere contributed to the value of $\overline{S}(Q)$. Moreover, an increased polydispersity led to an increased $\overline{S}(Q=0)$ and influenced the determination of the effective charge. $\overline{S_{eff}}(Q)$ is the weighted sum of the partial structure factors, and each component of the polydisperse system is weighted by a factor $x_i^{1/2} f_i(Q)$, which scales optically to homogeneous spheres to the third power. Accordingly, the resulting effects on the principal peak from the intrinsic size polydispersity were broadening, a reduction in height, and a shift in position to a lower wavenumber. These effects were examined by analyzing the contributions of each individual partial structure factor $S_{ij}(Q)$ of the subcomponent on the average structure factor $\overline{S}(Q)$. By analyzing the data in this way, no significant lowering or broadening of the $\overline{S_{eff}}(Q)$ peak was observed. This supported the premise that the six $S_{ij}(Q)$ values were not out of phase and reinforced the case for low sample charge polydispersity. Therefore, evidence was provided that any influence on the principal peak was minor; however, charge polydispersity did affect the width of the $\overline{S_{eff}}(Q)$ peak. Keeping the effective charge and the particle-number density fixed (n_{fit}); no significant changes were detected in either the peak height or the peak position of $\overline{S_{eff}}(Q)$ at small values of Q. Another indication of low polydispersity was the absence of a decrease in height of the $\overline{S_{eff}}(Q=0)$ peak, also indicating that the other components did not contribute significantly to the scattered intensity results. When the ionic strength was increased, consistent physical results were produced for the values of $\overline{S_{eff}}(Q)$ and $I_p(Q)$. If a charge renormalization was performed, the effective charge was found to be much smaller than both the structural charge and the conductivity charge. The structural charge found for the 70 nm particle was (1245 ± 190), the conductivity charge was (470 ± 100), and the effective charge was (390 ± 120) (Table 1). It was further established that the height of the principal $S_{exp}(Q)$ peak was higher than that of the peak obtained from the curve fit, resulting in higher effective charges. Monte Carlo simulations revealed that the effective charges were higher by a maximum of 9.5%. For the calculation of $\overline{S_{eff}}(Q)$, when comparing $\overline{S_{eff}}(Q)$ with $S_{exp}(Q)$, the charge Z_μ of component μ was taken into consideration because Z_μ scales with a_μ^2. The values of $S(Q)$ were calculated for $Z_\mu \propto a_\mu$ keeping the average charge

constant. Furthermore, no significant charge polydispersity was detected with respect to the width and the height of the 110 peak. Here was a strong indication that the polydispersity for the lipid A−diphosphate clusters for these particle-number densities was low and it did not influence the derived values of $\overline{z_{eff}}$. The influence of the charge polydispersity on the lipid A−diphosphate clusters was also considered. Therefore, by varying only μ and keeping all other parameters fixed, it was found that the charge polydispersity influenced the width of the $\overline{S_{eff}}(Q)$ peak. The increase in the height of the $S_{exp}(Q)$ peak to above 2.85 was *not* due to polydispersity, even though a small amount of charge polydispersity was present in the dispersions.

D. Surface Charge. The particle surface charges of the lipid A−diphosphate dispersions were determined by a comparison of the $S(Q{=}0)$ and $I_P(Q)$ curves for n as a function of c_S. The experimental and theoretical MCM results are presented in Figure 6A and B (Table 1). Interparticle interactions gave rise
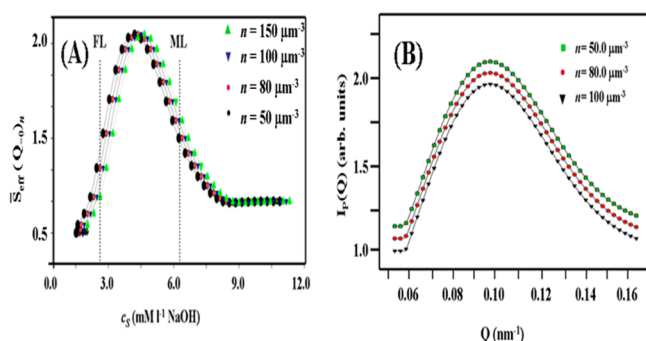
Figure 6. (A) Profiles from $S_{eff}(Q{=}0)_n$ values normalized for a lipid A−diphosphate cluster at $d = 70.0$ nm, for an effective charge $z_{eff} = 390$, and for a relative number density = 1, 2, 1 (thin solid lines). These plots were obtained using the MCM approach for different particle-number densities, n, as a function of c_S. FL and ML are the estimated freezing and melting lines of the lipid A−diphosphate clusters at 25 °C. (B) The corresponding particle form factor $I_P(Q)$ vs Q profiles obtained from SAXS measurements (▼, ●, ■) for various particle-number densities, n, and for $c_S = 5.15$ mM·L^{-1}. The theoretical $I_P(Q)$ vs Q profiles (solid lines) using the same parameters given in part A and using the MCM approach.

to the greatest influence at the limit of $\overline{S_{eff}}(Q{=}0)$. The fit to the limit in the simulation of both $\overline{S_{eff}}(Q{=}0)$ (Figure 6A) and the main peak of $I_P(Q)$ with the particle charge showed that the physical description of the lipid A−diphosphate cluster was appropriate to a first approximation (Figure 6B). Small errors in the ionic strength had little effect on the dispersions containing the lipid A−diphosphate cluster. This was because particle interactions decreased with increasing ionic strength and, accordingly, $I_P(Q)$ was little affected by the choice of the ionic strength. The simulation of $I_P(Q)$ was only marginally affected by the choice of the ionic strength. The experimental effective charge at the highest NaOH concentration used (5.0 × 10^{-5} M) was determined to be $Z^* = 215$. This charge value was significantly lower than the saturation value of ~600 predicted by the PBC model. It was found that for $Z^* = 390$ using the linearized PBC equation the predicted effective cluster charge values were 170 at 50 mM·L^{-1} NaOH and 300 at 100 mM·L^{-1} NaOH. At a constant particle-number density, the bare charge increased with c_S, predominantly because of an increased pH (4.5 ≤ pH ≤ 7.0). In this study, the actual numbers of dissociated phosphate groups of the lipid A−diphosphate were

smaller than $\overline{z_{surf}}$. This was because $\overline{z}$ was estimated from $\overline{z_{surf}}$ assuming a charge regulation for the PBC model and using the mass equation:

$$R{-}H_2PO_4^- = [H^+]_S \cdot \alpha/(1 - \alpha) \tag{13}$$

In the equation, $[H^+]_S$ is the H$^+$ concentration close to the lipid A−diphosphate cluster surface, and $\alpha = \overline{z}/z_{surf}$ is the degree of dissociation. The values computed from the particles studied were $-\ln[H^+]_S = 2.15$ and $\overline{z} = 390$. The $R{-}H_2PO_4^-$ value appeared to be reasonable, considering that the $R{-}H_2PO_4^-$ groups were not freely available in the dispersion but bound to the cluster surface. Therefore, a relatively low degree of dissociation was to be expected ($\alpha \sim 0.005$) and the obtained pK_{a1} was confirmed.

In the crystalline bcc region, $\overline{S_{eff}}(Q{=}0)$, there was a higher dependency on an increased particle-number density, n, than for further NaOH additions. There was also an increase in the value z_{eff} along the melting line, which approached equilibrium at $c_S = 6.0$ mM L^{-1}. The z_{eff} value was higher than that found in the fluid state prior to freezing.

Therefore, under either deionized or low c_S conditions, $\overline{z_{eff}}$ remained constant at 300 ± 75. The experimental results obtained from the $\overline{S_{eff}}(Q{=}0)$ and $I_P(Q)$ vs Q profiles together with numerical calculations revealed that $(\overline{z_{eff}}, m)$, the effective charge along the melting line, was always larger than $\overline{z_{eff}}$ for the fluid state prior to freezing ($c_S = 0.02{-}0.075$ mM·L^{-1}). However, z_{eff}, m along the melting line was always lower than $\overline{z_{eff}}$ for the fluid state (right boundary in Figures 7 and 8).

The following comments are submitted here so that a comparison may be made between this study using NaOH and previous investigations utilizing NaCl.[52,54] The crystallization of
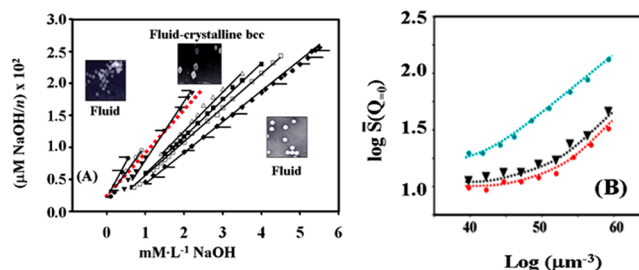
Figure 7. (A) An experimental phase diagram of charged spherical lipid A−diphosphate clusters where the ratio of μM NaOH, associated with the particles, and the particle-number density, n, is plotted against the NaOH concentrations for $n = 44$ (●), 66 (○), 80 (▼), 118 (△), 158 (■), 185 (□), and 215 (◆) in μm^{-3} ($T = 25$ °C). The red dotted line indicates the equivalent titration points. The insets depict the particles at the fluid states, left $d = 7.0$ nm and right $d = 70$ nm, respectively, and the 100 nm sized lipid A−diphosphate crystals (see Figure 2). The red dotted line shows the equivalent titration points. The insets are TEM photographs of nanometer sized lipid A−diphosphate crystals (see Figure 2) from the fluid states, left $d = 7.0$ nm and right $d = 70$ nm, and the insets depict the particles at the fluid states, left $d = 7.0$ nm and right $d = 70$ nm, respectively, and the 100 nm sized lipid A−diphosphate crystals (see Figure 2). The existence of two phases is shown by the horizontal bars. In part B, $\overline{S_{eff}}(Q{=}0)_n$ normalized by the value $S_{eff}(Q{=}0)$ for a particle $d = 70.0$ nm and an effective charge $z_{eff} = 390$ ($c_S = 6.0$ mM·L^{-1}) for the different particle-number densities (n) at the left phase boundary (▼) and at the right phase boundary (red ●), under conditions of maximum interaction (teal ●). The lines are theoretical fits to the experimental data with $z_{eff} = 315 ± 26$ for the left boundary and $z_{eff} = 340 ± 30$ for the right boundary at maximum interaction.
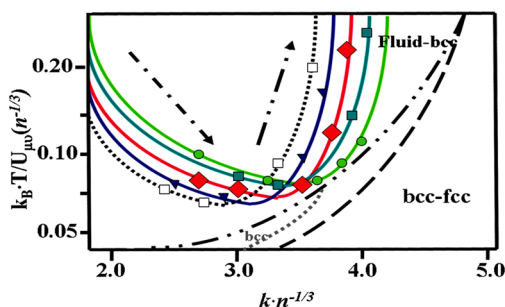
Figure 8. Phase diagram plotted as $k_BT/U_{\mu\nu}(n^{-1/3})$ vs $\kappa \cdot n^{-1/3}$ of charge-variable lipid A−diphosphate clusters from aqueous dispersions simulated from the experimental data according to RKG.[28] With an increase in n and at maximum interaction, the corresponding state lines are calculated for the maximum effective charge, $z_{eff} = 478$. The other state lines for constant n and increasing c_S correspond to an increase in surface charge (left lines and down arrow) and screening (right lines and up arrow). Equilibrium-state lines for phase boundaries with maximum interaction are shown as (·—) and (— —). The gray squared boundary shows the crystalline bcc phase. Equilibrium-state lines are shown as colored thin lines for constant particle-number densities n: (···) 60.0 μm^{-3}, (blue line) 90.0 μm^{-3}, (red line) 130.0 μm^{-3}, (teal line) 157.0 μm^{-3}, and (green line) 251.0 μm^{-3}. The symbols □, ▼, ◆, ■, and ● correspond to the observed melting transitions at maximum interaction by increasing NaOH at constant n: 60.0, 100.0, 120.0, 140.0, and 240.0 μm^{-3}, respectively.

lipid A−diphosphate clusters at low ionic strength, $I \sim 10^{-4}$ M NaCl, commenced at volume fractions ϕ as low as $\phi = 3.5 \times 10^{-4}$. Conversely, the crystallization of lipid A−diphosphate clusters at the same ionic strength in the presence of mM·L^{-1} NaOH commenced at volume fractions of $\phi = 2.52 \times 10^{-2}$ because of many-body effects. The solubility of lipid A−diphosphate clusters in the presence of $\sim 10^{-4}$ M NaCl was for $c = 4.4$ mg/cm^3, but the solubility of lipid A−diphosphate clusters in the presence of 0.5−1.0 mM·L^{-1} NaOH was for $c = 32-42$ mg/cm^3. The phases observed for lipid A−diphosphate, after the removal of excess NaCl, with $\sim 10^{-4}-10^{-3}$ M NaCl remaining were purely electrostatic, with low contributions arising from many-body effects. In the case of the lipid A−diphosphate clusters in the presence of mM·L^{-1} NaOH, the acquired results were interpreted in terms of many-body effects. The existence of a lipid A−diphosphate metastabile phase was not detected in the titration experiment using NaOH. A dramatic crystal growth was observed at the free boundary in the presence of mM·L^{-1} NaOH where 7 nm particles assembled to form a body centered cubic (bcc) unit cell with a lattice parameter of $a = 37.5$ nm. This was not observed for the lipid A−diphosphate clusters in the presence of mM·L^{-1} NaCl. A face centered cubic (fcc) structure formed with an increase in the particle-number density in the presence of mM·L^{-1} NaCl. This was in contrast to the present study, where an increase in mM·L^{-1} NaOH concentration led to a self-assembly of the 7 nm lipid A−diphosphate structures which formed bcc crystals followed by the appearance of 70 nm clusters in the fluid state.

A dramatic crystal growth was observed at the free boundary in the presence of mM NaOH where 7 nm particles assembled to form a body centered cubic (bcc) unit cell with a lattice parameter of $a = 37.5$ nm. This was not observed for the lipid A−diphosphate clusters in the presence of mM NaCl. There was also a face centered cubic (fcc) structure present with an increase in the particle-number density in the presence of mM

NaCl. This was in contrast to the present study, where an increase in mM·L^{-1} NaOH concentration led to a self-assembly of the 7 nm lipid A−diphosphate structures which formed bcc crystals followed by the appearance of 70 nm clusters in the fluid state.

E. Phase Diagram. Presented in Figure 8 is an experimental phase diagram of charged spherical lipid A−diphosphate clusters where the particle-number density, n, is plotted against the NaOH concentration. The phase diagram shows that a fluid phase first became an ordered-crystalline (bcc) phase and thereafter a fluid phase formed with an increase in the c_S. The NaOH additions were determined from conductivity measurements at known n values. With the formation of colloidal crystal, the fluid phase became bcc ordered (Figure 3). It was established that following the addition of mM·L^{-1} NaOH there was an increase in particle charge and freezing occurred. However, with additional amounts of NaOH, an increase in the lipid A−diphosphate particle charge took place, as well as a re-entry into the fluid phase. The mM·L^{-1} NaOH addition resulted in an increase in the bare charge Z, the conductivity charge Z^*, and the effective charge $\overline{z}_{eff}$. In Figure 8, it was observed that melting occurred as a consequence of charging on the left equilibrium-state boundary and as a result screening on the right state boundary, when a fluid structure was encountered. The diffraction results obtained at $c_S \cong 3.2$ mM·L^{-1} disclosed an assembled bcc−cubic lattice with a unit cell $a = 36.4$ nm. Investigations are in progress on structures formed at high n ($\sim 400 \, \mu m^{-3}$) and c_S (4.0 mM·L^{-1} $\leq c_{NaOH}$ 7.0 mM·L^{-1}). Preliminary findings showed the presence of an fcc cubic crystal structure and a morphological change occurred at $c_S \cong 25$ mM·L^{-1}, which led to a rod-like structure previously reported.[73] If the mM·L^{-1} NaOH was increased, there was a corresponding increase in charge on the self-assembled lipid A−diphosphate particles according to R−H$_2$PO$_4$H + OH$^-$ → R−HPO$_4^-$ + H$_2$O. At low mM·L^{-1} NaOH concentrations c_S, the lipid A−diphosphate retained a bcc structure. However, with additional increases in the mM·L^{-1} NaOH, the interactions became screened with neither an increase nor a decrease in charge and the system began to melt (Figures 3 and 6). This was confirmed by both static, dynamic light scattering and diffraction for lipid A−diphosphate particles whose diameters were 70 nm (unpublished results 2008). Although the lipid A−diphosphate samples investigated covered a limited pH range (4.5 ≤ pH ≤ 7.5), there was a sufficient excess of NaOH to attribute the occurrence of melting to added screening produced by the excess. For silica and latex systems, Yamanaka et al.[34] showed that when charging took place the melting behavior was attributed to the self-screening effect.

In the construction of the phase diagram, both phase boundaries were established according to RKG,[28] through the use of the effective charge, $\overline{z}_{eff}$, and the conductivity charge, Z_σ (Figure 8). The screened Debye−Hückel potential[14,28] ($k_B \cdot T/U_{\mu\nu}(n^{-1/3})$ was plotted as a function of $kn^{-1/3}$, where $U_{\mu\nu}$ was calculated from eq 9 for each n and where k is the screening parameter $k = 4\pi k_B \cdot T \cdot \lambda_B(nZ_{eff} + 2 \times 10^3/N_A \cdot c_S)^{1/2}$ and $\lambda_B = 0.735$ nm (Bjerrum length). Calculation and simulations of both phase boundaries disclosed that the mean effective charges were $\overline{z}_{eff} = 315 \pm 26$ at the left boundary, the fluid crystalline bcc interface. At the right boundary between the crystalline phase and the fluid phase, the mean effective charge was $\overline{z}_{eff} = 340 \pm 30$. The bare-surface-charge density was $\sigma = 4.5 \, \mu S/cm^{-2}$, a much smaller value than previously found for lipid A−diphosphate particles corresponding to $Z = 1245$. The total

surface density was determined to be $\sigma_T = 0.15$ C/m^2. It was deduced from Figure 8 that if the particle-number density remained constant and the NaOH concentration was increased, the particle-interaction potential, $U \cdot (n^{-1/3})$, rose as a result of an increased particle surface charge. Because of the lipid A–diphosphate counterions, the screening parameter, κ, increased steadily if the particle-number density, $n^{-1/3}$, remained constant. As a result, a decrease in the equilibrium-state lines was observed and the melting line was reached. This accounted for the maximum interaction equilibrium state line when the surface charges approached their highest value. Consequently, any further addition of mM·L^{-1} NaOH screened the lipid A–diphosphate particle surface charge and initiated a reduction in the particle–particle interaction. The screening parameter, κ, then depended only on the screening electrolyte (NaOH). The result was an increase in the equilibrium state lines which again reached the melting line. From the phase behavior of the charge-variable lipid A–diphosphate spherical assemblies presented in Figures 6 and 7, it was concluded that for this system the location of the melting transition could be accurately simulated. If the effective charges, which account for both counterion condensation and macroions, were applied, the observed fluid phase also explained the excess electrolyte.[9,10] Furthermore, the melting line was reached by the fluid–bcc line. The right and left phase boundaries were in accordance with the RKG theory, and no significant differences were detected by using either the RKG or the MF procedures.[28,29]

The morphological phase transitions of the lipid A–diphosphate clusters during titration with mM·l^{-1} at various n were diagrammatically represented in Figure 9A. Figure 9B

Figure 9. (A) A representation of the smallest lipid A–diphosphate cluster for $d = 7.0$ nm observed regularly in TEM images at particle-number densities of $n \cong 10$–$100\ \mu m^{-3}$ and $c_S = 0.02$–2.0 mM L^{-1} at 25 °C. Body-centered cubic crystals with a lattice constant $a = 35.6$ nm appear at the higher values of n and at the indicated c_S. With an increase in $c_S \geq 5.25$ mM·L^{-1} and at a constant particle-number density, the lipid A–diphosphate crystals melt. The fluid phase which forms contains lipid A–diphosphate clusters with a diameter of $d = 70$ nm (size bar 70 nm). (B) The scaling plot of SAXS intensities vs Q/Q_{max} for lipid A–diphosphate clusters. $n = 160\ \mu m^{-3}$ at different c_S values for $Q_{max} = 0.39$ nm reveal a bcc–fluid transition. The dashed line is the resolution curve (blue - - -).

underlines the existence of a bcc–fluid phase transition at different c_S by using the Debye correlation function $\gamma(r)$.[74] The SAXS intensity profiles reflect the local structures of the self-assembled lipid A–diphosphate clusters around the single peak, the Q_{max} (110 peak). For a two phase system comprised of a crystalline bcc and a fluid phase which contains lipid A–diphosphate clusters in solution, the intensity distribution is proportional to a three-dimensional Fourier transform of the

Debye correlation function $\gamma(x)$. Using a scaled Debye correlation function following the notation of Chen et al.[75] (eq 14):
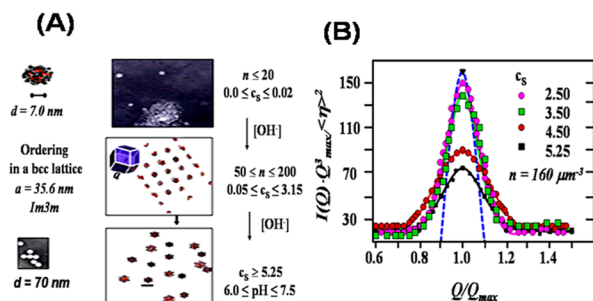
$$\frac{I(Q) \cdot Q_{max}^3}{\langle \eta^2 \rangle} = \int_0^\infty 4\pi x^2\ dx J_0(xy)\gamma(x) \tag{14}$$

Here, $1/Q_{max}$ is the mean distance between lipid A–diphosphate clusters, $\gamma(r \cdot Q_{max})$ is the correlation function, $x = Q_{max}r$, $y = Q/Q_{max}$, $\langle \eta^2 \rangle$ is known as the invariant of scattering,[73] and J_0 is the Bessel function of zero order. Therefore, if they were present, it would be possible to detect local changes associated with different phases for various c_S. In Figure 9B, the SAXS profiles obtained for various c_S concentrations within the single phase region were superimposed on one master curve. When examining the diffraction peak width as a function of c_S, two distinct degrees of order existed in the dispersion at $n = 160\ \mu m^{-3}$. The narrow peak widths observed at $c_S = 2.5$ and 3.5 mM·L^{-1} were resolution limited and were attributable to the crystalline bcc structure where interparticle distances were the same. The broad peak represents the fluid state, which is more diffuse than the resolution peak. This was also consistent with the view of a crystalline-to-liquid transformation of self-assembled lipid A–diphosphate clusters. For NaCl additions, the structure factor reaction was through the diffusive double layer repulsion of the lipid A–diphosphate clusters. For additions of NaOH, the response of the structure factor $S(Q)$ was attributed to an anion exchange mechanism and many-body effects through macroion shielding.

The self-assembly of the lipid A–diphosphate with the addition of mM·L^{-1} NaOH occurred spontaneously at ambient temperatures and at low volume fractions. For this system, neither sonication nor heating at 50 °C for extended periods of time (~1 h) were necessary to promote crystallization. Because of the inherent low polydispersity in shape, mass, and charge, the crystalline lipid A–diphosphate phase formed rapidly when NaOH was added, indicative of short time scale kinetics. The long time scale kinetics and the relaxation process rest on ordering in the fluid state, freezing in the crystalline bcc state, and finally melting with further additions of NaOH. This is markedly different from the formation of DNA–Ca^{2+}–zwitterionic lipid complexes.[76,77] The lipid A–diphosphate is not a zwitterionic molecule (anionic), and the addition of NaOH promoted the formation of a second fluid phase with 70 nm particles as a result of many-body interactions. The many-body effect facilitated the reorganization of the lipid A–diphosphate molecules for the self-assembly. This type of phase was not detected in the DNA–Me^{2+}–zwitterionic lipid systems.

IV. CONCLUSIONS

When the c_S (mM·L^{-1}) was increased, a new fluid phase of self-assembled lipid A–diphosphate formed, followed by the development of a fluid ordered-crystalline bcc phase. For sufficiently large values of n, lipid A–diphosphate crystallized through an increase in Z_{eff} at constant c_S. If the c_S was increased further, the crystals melted with little change in Z_{eff} and the difference between $2d_{exp}$ and $2d_{calc}$ became slightly larger. This was a consequence of an increased counterion condensation and many-body effects. Both of the effects contributed to the enhancement of the interparticle interaction and attraction. The presence of NaOH in the lipid A–diphosphate aqueous dispersions stabilized the two-state structure. The stabilizing

effect was promoted by long-range (counterion mediated) attractive interactions between the clusters and the many-body effects. The lipid A−diphosphate clusters also underwent a fluid−order transition and an order−fluid transition. When c_S and n were increased, the length scale of the repulsion decreased because of many-body effects, and a disorder−order transition occurred at n close to the freezing transition. At lower particle-number densities, as the length scale of the repulsive forces increased, the fluid−crystalline transition gave rise to bcc-type crystals.[78] This showed that self-screening was much smaller than in previous studies.[53,55] Experimental observations and simulations using the MCM approach supported the existence of a transition from a fluid phase to a bcc phase. The expected lipid A−diphosphate fcc structure found in the presence of 5.0 mM·L^{-1} NaCl was not detected in this investigation. In previous research, a glassy phase was found with the addition of 1.0−10 μM HCl solution (pH 2.5).[55] However, no such phase was encountered in these experiments where NaOH was used to promote the self-assembly of lipid A−diphosphate clusters. Furthermore, there was no fcc structure for 0.05 mM·L^{-1} ≤ c_S ≤ 5.5 mM·L^{-1}, but there was a crystalline bcc phase present between the two clearly defined fluid phases. It was unusual to encounter a bcc structure for ionic strengths of different magnitude (5.0 mM·L^{-1} vs 0.5 mM·L^{-1} NaOH) and for the same n, demonstrating that the OH$^-$ ions contributed to the scenario. It is also feasible that the structural transition path was influenced by topological dissimilarities because of altered elastic deformations between the crystalline bcc phase which formed and the fluid phases from which it originated.

■ AUTHOR INFORMATION

Corresponding Author

*E-mail: hparadies@aol.com (H.H.P.) or c.a.faunce@salford.ac.uk (C.A.F.).

Notes

The authors declare no competing financial interest.

■ ACKNOWLEDGMENTS

■ REFERENCES

(1) Levin, Y. Rep. Prog. Phys. 2002, 65, 1577−1587.
(2) Reinke, D.; Stark, H.; von Grünberg, H. H.; Schofield, A. B.; Maret, G.; Gasser, U. Phys. Rev. Lett. 2007, 98, 03830−03835.
(3) Okubo, T. ACS Symp. Ser. 1994, 548, 364−380.
(4) Yethiraj, A. Soft Matter 2007, 3, 1099−1103.
(5) Luck, W.; Klier, M.; Wesslau, H. Ber. Bunsen-Ges. Phys. Chem. 1963, 67, 84−94.
(6) Larsen, A. E.; Grier, D. G. Nature (London) 1977, 385, 230−233.
(7) Hiltner, P. A.; Krieger, I. M. J. Phys. Chem. 1969, 73, 2386−2389.
(8) Monovaukas, Y.; Gast, A. P. J. Colloid Interface Sci. 1989, 128, 533−548.
(9) Ise, N. Ber. Bunsen-Ges. Phys. Chem. 1996, 100 (6), 841−846.
(10) Okubo, T.; Kiriyama, K. Ber. Bunsen-Ges. Phys. Chem. 1996, 100, 849−856.
(11) Sirota, E. B.; Ou-Yang, H. D.; Sinha, S. K.; Chaikin, P. M.; Axe, J. D.; Fujii, Y. Phys. Rev. Lett. 1989, 62, 1524−1529.
(12) Schmitz, K. S. Phys. Chem. Chem. Phys. 1999, 1, 2109−2119.
(13) Yamanaka, J.; Hayashi, Y.; Ise, N.; Yamaguchi, T. Phys. Rev. E 1997, 55, 3028−3036.

(14) Wette, P.; Klassen, I.; Holland-Moritz, D.; Herlach, D. M.; Schöpe, H. J.; Lorenz, N.; Reiber, H.; Palberg, T.; Roth, S. V. J. Chem. Phys. 2010, 132, 131102−131107.
(15) Alexander, S.; Chaikin, P. M.; Grant, P.; Morales, G. J.; Pincus, P. A.; Hone, D. J. J. Chem. Phys. 1984, 80, 5776−5782.
(16) Bucci, S.; Fagotti, C.; Degiorgio, V.; Piazza, P. Langmuir 1991, 7, 824−826.
(17) Belloni, L. Colloids Surf., A 1998, 140, 227−243.
(18) Gisler, T.; Schulz, S. F.; Borkvec, M.; Sticher, H.; Schurtenberger, P.; D'Aguanno, B.; Klein, R. J. Chem. Phys. 1994, 101, 9924−9934.
(19) Belloni, L. Chem. Phys. 1985, 99, 43−53.
(20) Thies, M.; Hinze, U.; Paradies, H. H. Colloids Surf., A 1995, 101, 261−271.
(21) Ito, K.; Nakamura, H.; Yoshida, H.; Ise, N. J. Am. Chem. Soc. 1980, 110, 6955−6960.
(22) Welch, P.; Muthukumar, M. Macromolecules 1998, 31 (17), 5897−5897.
(23) Ohsima, A.; Konishi, T.; Yamanaka, J.; Ise, N. Phys. Rev. E 2001, 64, 051808−051817.
(24) Ise, N.; Okubo, T.; Sugimura, M.; Itoh, K.; Nolte, J. J. Chem. Phys. 1983, 78, 536−545.
(25) Quesada-Perez, M.; Callejas-Fernandez, J. R.; Hidalgo-Alvarez, R. Phys. Rev. E 2000, 61, 574−582.
(26) McConnell, G. A.; Gast, A. P.; Huang, J. S.; Snell, S. D. Phys. Rev. Lett. 1993, 71, 2102−2105.
(27) Trizac, E.; Levin, Y. Phys. Rev. E 2004, 69, 031403−031407.
(28) Robbins, M. O.; Kremer, K.; Grest, G. S. J. Chem. Phys. 1988, 88, 3286−3313.
(29) Meijer, E. J.; Frenkel, D. J. Chem. Phys. 1991, 94, 2269−2272.
(30) Hamaguchi, S.; Farouki, R. T.; Dubin, D. H. Phys. Rev. E 1997, 56, 4671−4682.
(31) Palberg, T.; Mönch, W.; Bitzer, F.; Piazza, R.; Bellini, L. Phys. Rev. Lett. 1995, 74, 4555−4560.
(32) Royall, C. P.; Leunissen, M. E.; Hynninen, A. P.; Dijkstra, M.; van Blaaderen, A. J. Chem. Phys. 2006, 124, 244706−244714.
(33) Klein, R.; von Grünberg, H. H.; Bechinger, C.; Brunner, M.; Lobashkin, V. J. Phys.: Condens. Matter 2002, 14, 7631−7648.
(34) Yamanaka, J.; Yoshida, H.; Koga, T.; Ise, N.; Hashimoto, T. Langmuir 1999, 15 (12), 4198−4202.
(35) Reinhardt, A.; Williamson, A. J.; Doye, J. P. K.; Carrete, J.; Varela, L. M.; Louis, A. A. J. Chem. Phys. 2011, 134, 104905−104917.
(36) Shapran, L.; Schöppe, H.-J.; Palberg, T. J. Chem. Phys. 2006, 125, 194714−194721.
(37) Adams, M.; Dogic, Z.; Keller, S. L.; Fraden, S. Nature (London) 1998, 393, 349−352.
(38) Dogic, Z.; Frenkel., D.; Fraden, S. Phys. Rev. E 2000, 62, 3925−3933.
(39) Kotra, L. R.; Golemi, D.; Amoro, N.; Liu, G. J.; Mohasbery, S. J. Am. Chem. Soc. 1999, 121 (38), 8707−8711.
(40) Raetz, C. R. H.; Whitfield, C. Annu. Rev. Biochem. 2002, 71, 635−700.
(41) Frecer, V.; Ho, B.; Ding, J. L. Eur. J. Biochem. 2000, 267, 837−847.
(42) Brandenburg, K.; Koch, M. H.; Seydel, U. J. Struct. Biol. 1990, 105, 11−19.
(43) Brandenburg, K.; Richter, W.; Koch, M. H.; Seydel, U. Chem. Phys. Lipids 1998, 91, 53−69.
(44) Alving, C. R. Immunobiology 1993, 187, 430−466.
(45) Garcia-Contreras, L.; Wong, Y.-L.; Muttil, P.; Padilla, D.; Sadoff, J.; DeRouse, J.; Germishouzen, W. A.; Gooonesekera, S.; Elbert, K.; Bloom.; et al. Proc. Natl. Acad. Sci. U.S.A. 2008, 105, 4656−4660.
(46) Weber, K.; Möller, K.; Welzeck, M.; Schorr, J. In Artificial Self-Assembling Systems for Gene Delivery; Felgner, P., Heller, M. J., Lehn, P., Behr, J. P., Szoka, F., , Jr., Eds.; Conference Proceedings Series, ACS, Sept 28−29 and Oct 10−11, 1995, Washington, DC, pp 31−40.
(47) Chan, S.; Horner, S. R.; Fauchet, P. M.; Miller, B. J. J. Am. Chem. Soc. 2001, 123 (47), 11797−11798.

13008

dx.doi.org/10.1021/jp306632q | J. Phys. Chem. B 2012, 116, 12997−13009

(48) Yang, L.; Ding, L.; Huang, H. W. *Biochemistry* **2003**, *42*, 6631−6636.

(49) Ding, L.; Yang, L.; Weiss, T. M.; Warring, A. J.; Lehrer, R. I.; Huang, H. W. *Biochemistry* **2003**, *42* (12), 12251−12259.

(50) Faunce, C. A.; Reichelt, H.; Paradies, H. H. *J. Phys. Chem. B* **2008**, *112*, 8859−8864.

(51) Hayashida, O.; Kato, M.; Akaiyi, K.; Aoyama, Y. *J. Am. Chem. Soc.* **1999**, *121* (49), 11597−11598.

(52) Li, C.; Budge, L. P.; Driscoll, C. D.; Willardson, B. W.; Allman, G. W.; Savage, P. B. *J. Am. Chem. Soc.* **1999**, *121* (5), 931−940.

(53) Faunce, C. A.; Paradies, H. H.; Quitschau, P. *J. Phys. Chem. B* **2003**, *107*, 2214−2227.

(54) Faunce, C. A.; Reichelt, H.; Quitschau, P.; Paradies, H. H. *J. Chem. Phys.* **2007**, *127*, 115103−115125.

(55) Reichelt, H.; Faunce, C. A.; Paradies, H. H. *J. Phys. Chem. B* **2008**, *112*, 3290−3293.

(56) Hansen, J.-P.; McDonald, L. R. *Theory of Simple Liquids*; Academic Press: New York, 2007.

(57) Belloni, L. *Chem. Phys.* **1985**, *99*, 43−53.

(58) Chang, J.; Lesieur, P.; Delsanti, M.; Belloni, L.; Bonnet-Gonnet, C.; Cabane, B. *J. Phys. Chem.* **1995**, *99*, 15993−16002.

(59) Rogers, F. J.; Young, D. A. *Phys. Rev. A* **1984**, *30*, 999−1007.

(60) Verweg, E. J. W.; Overbeck, J. Th. G. *Theory of the Stability of Hydrophobic Colloids*; Elsevier: New York, 1948.

(61) Henry, N. F. M., Lonsdale, K., Eds. *International Tables for X-Ray Crystallography*; The Kynoch Press: Birmingham, U.K., 1965; Vol. *1*. In the new ed., International Tables for Crystallography; Hahn, T., Ed; D. Reidel Publishing Co.: Dordrecht, The Netherlands, 1983.

(62) Warren, B. E. *J. Appl. Phys.* **1941**, *12*, 375−385.

(63) Jacobs, C. W.; Warren, B. E. *J. Am. Chem. Soc.* **1937**, *59* (12), 2588−2591.

(64) Stokes, A. R.; Wilson, A. J. C. *Proc. Cambridge Philos. Soc.* **1942**, *38*, 313−322.

(65) Harkless, C. A.; Singh, M. A.; Nagler, S. E.; Stephenson, G. B.; Jordan-Sweet, J. L. *Phys. Rev. Lett.* **1990**, *64*, 2285−2290.

(66) Verlet, L.; Hansen, J.-P. *Phys. Rev.* **1969**, *184*, 151−161.

(67) Löwen, H.; Palberg, T.; Simon, R. *Phys. Rev. Lett.* **1993**, *70*, 1557−1560.

(68) Brock, J. D. Bond-Orientational Order. In *Bond-Orientational Order in Condensed Matter Systems*; Strandburg, K., Ed.; Springer-Verlag: New York, Berlin, Heidelberg, 2012; pp 1−31.

(69) Lindemann, F. A. *Z. Phys.* **1910**, *11*, 609−612.

(70) Fisher, M. E.; Burford, R. J. *Phys. Rev.* **1967**, *156*, 583−622.

(71) Agnon, N. *Chem. Phys. Lett.* **2000**, *319*, 247−252.

(72) Phalakarnkul, J. K.; Gast, A. P.; Pecora, R.; Nägele, G.; Farrante, A.; Mandl-Steinninger, B.; Klein, R. *Phys. Rev. E* **1993**, *47*, 2562−2574.

(73) Faunce, C. A.; Paradies, H. H. *J. Chem. Phys.* **2008**, *128*, 065105−065113.

(74) Guinier, A. *X-Ray Diffraction*; W. H. Freeman & Company: San Francisco, CA, London, 1963.

(75) Chen, S.-H.; Chen, W.-R.; Mallamace, F. *Science* **2003**, *300*, 619−624.

(76) McManus, J. J.; Rädler, J. O.; Dawson, K. A. *J. Am. Chem. Soc.* **2004**, *126*, 15966−15967.

(77) McManus, J. J.; Rädler, J. O.; Dawson, K. A. *Langmuir* **2003**, *19*, 9630−9637.

(78) Shih, W. Y.; Aksay, I. A.; Kikuchi, R. *J. Chem. Phys.* **1987**, *86*, 5127−5133.